



## **EXPERIMENTAL IDENTIFICATION OF FLOW TURBULENCE EXCITATIONS IN A FUEL BUNDLE TEST RIG: PART 2 - FLOW MEASUREMENTS AND VIBRATION COMPUTATIONS FOR VALIDATION**

**Valérie Biscay<sup>1</sup>, Xavier Delaune<sup>2</sup>, Philippe Piteau<sup>2</sup>, Serge Delafontaine<sup>1</sup>, José Antunes<sup>3</sup>,  
and Vincent Faucher<sup>4</sup>**

<sup>1</sup> Research engineer, Den-Département Technologie Nucléaire (DTN), STCP, LHC, CEA Cadarache, F-13115 Saint-Paul-lez-Durance, France

<sup>2</sup> Research engineer, Den-Service d'études mécaniques et thermiques (SEMT), CEA, Université Paris-Saclay, F-91191, Gif-sur-Yvette, France

<sup>3</sup> Research engineer, IST-Centre for Nuclear Sciences and Technologies (C2TN), Estrada Nacional 10, 2695-066 Bobadela LRS, Portugal

<sup>4</sup> Project manager, Den-Département Technologie Nucléaire (DTN), DIR, CEA Cadarache, F-13115 Saint-Paul-lez-Durance, France

### **ABSTRACT**

In a companion paper (Part 1 - Antunes et al., 2017) results were presented from experiments aiming at the identification of turbulence excitation, performed on a 5x5 bundle subjected to axial flow. The experimental data consisted on transverse velocity responses measured at several locations along the instrumented rod. Due to the considerable stiffness of the system, the measured vibration amplitudes were found to be quite low, leading to problematic data. Nevertheless, plausible identification results were obtained, by developing a highly constrained identification scheme. In order to assert the quality of the identification results, complementary measurements and computations are performed as follows: (1) Laser Doppler Velocimetry (LDV) of the flow in the vicinity of the tested tube; (2) Time-domain dynamical computations based on the identified flow excitation. Concerning the LDV measurements, the axial component and one cross component of the flow velocity are measured simultaneously and their mean values computed. The depth of the measured flow volume is adjusted by focalization of the laser beams. For each measurement plane along the rod, velocity is sensed in the inter-rods flow channels and between the outer rods and the test section walls. Overall, the measured flow velocity profiles are compatible with the identified profile in Part 1. On the other hand, time-domain computations are performed by exciting the rod model with a simulated turbulence field stemming from the identified flow excitation. The vibratory responses thus computed are compatible with the measured vibration data in Part 1. These complementary measurements and dynamical computations further enlighten and validate the identified flow excitation features.

### **INTRODUCTION**

As argued in a companion paper (Part 1 - Antunes et al., 2017), for multi-supported tubular components, the correct identification of the flow excitation spectral content and spatial distribution are crucial for the predictive analysis of nuclear components, such as steam generator tubes and fuel rods. The excitation features are typically obtained from experiments and, when the random forces are indirectly inferred from the system vibratory responses, their identification involve the solution of a delicate inverse problem. Obtaining satisfactory results in case of problematic and noisy signals remains a challenge, which was addressed in Part 1 by developing and applying a highly constrained identification formulation.

Results were presented from preliminary experiments aiming at the identification of turbulence forces performed on a 5x5 bundle subjected to an axial flow with average velocity of 5 m/s. The experimental data consisted on transverse velocity responses measured at several locations along the instrumented rod, which were sensed using a two-channel laser vibrometer. The measured RMS amplitudes were found to be quite low, leading to noisy experimental data. Moreover, nonlinear contact/friction effects at the supporting grids, as well as coupling between the two orthogonal motion directions, among the additional difficulties of these experiments. As a result, the test data collected posed a considerable challenge for source identification. Nevertheless, seemingly plausible results have been identified from our constrained identification scheme. In order to assert the quality of the identification results, complementary measurements and computations have been latter performed and are reported here, as follows: (1) Flow velocity measurements in the vicinity of the tested tube along the bundle axis; (2) Time-domain dynamical computations based on the identified flow excitation.

Flow velocity measurements are obtained by Laser Doppler Velocimetry, seeding the fluid with small tracer particles. Then, any flow volume of interest is targeted with two coherent laser beams, leading to an interference image, the resultant light intensity frequency enabling measurement of the particles velocity at any given focalization depth. Measurements are performed at several cross-planes along the bundle, including the highly excited region near the flow entrance, in the inter-rods flow channels as well as between the outer rods and the test section walls. Overall, the measured flow velocity profiles are fully compatible with the identified profile in Part 1.

On the other hand, all aspects of the tested configuration are modelled and time-domain numerical computations performed by exciting the rod model with a simulated turbulence excitation stemming from the identified flow velocity profile and reduced excitation spectrum. The vibratory responses thus computed are compatible with the measured vibration data, provided that adequate damping is encapsulated in the computational modal basis. In conclusion, these complementary measurements and dynamical computations further enlighten and validate the identified flow excitation features presented in Part 1.

## FLOW VELOCITY MEASUREMENTS

### *Experimental setup*

**Test rig and instrumentation:** The experiment is performed in the MERCURE facility, located at CEA Cadarache, France. It consists in a primary hydraulic loop, a secondary cooling loop and a test section implementing two reduced scale fuel assemblies (5x5 bundles). Details are given in (Part 1 - Antunes et al., 2017) introducing the vibratory measurements of one selected instrumented rod.

Concerning velocity measures in the fluid, Laser Doppler Velocimetry is used to acquire the velocity of particles moving in the fluid of interest (see Figure 1). Provided the particles are small and light enough, their velocity can be assumed to be the velocity of the fluid itself. The physical principle used to measure the velocity is the scattering of light by the particles. The intersection of two laser beams results in a fringe pattern (a series of light and dark fringes). As a particle moves through the measuring volume, it scatters light when it crosses a bright fringe, and scatters no light as it passes a dark fringe. This results in a fluctuating pattern of scattered light intensity with a frequency proportional to the particle velocity. Since the distance between fringes and the time for the particle to go from one fringe to the next (inverse of signal frequency) are known, the measured signal frequency can be converted to velocity. For further details, see for instance Eder et al. (2001).

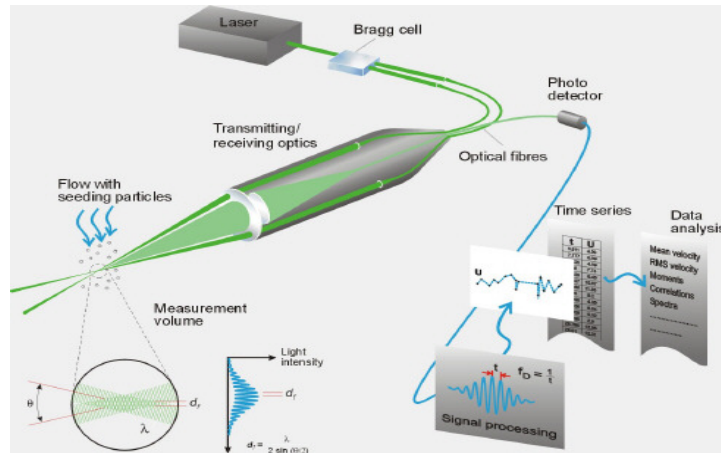


Figure 1. Basic principle for Laser-Doppler Velocimetry.

**Velocimetry protocol:** Axial component and one cross component of the flow velocity are measured simultaneously (in match mode) by two yellow beams ( $\lambda = 561 \text{ nm}$  for axial flow) and two green beams ( $\lambda = 532 \text{ nm}$  for cross flow) respectively. Leaving the optical probe, the distance between the two yellow beams was 50 mm and 13 mm for the two green beams. One of the two laser beams is frequency shifted by a Bragg cell by 40 MHz. As the focal length used is 363 mm, the corresponding measurement volumes respectively have dimensions in water along dX, dY and dZ of  $0.11 \times 0.11 \times 1.90 \text{ mm}$  for yellow beams and  $0.11 \times 0.11 \times 6.93 \text{ mm}$  for green beams. The dZ length of the measurement volume in water in match mode corresponds to the intersection of the yellow and green volume, i.e. dZ of 1.90 mm.

The measurement points are positioned between the rod rows by a micrometric displacement table along 3 axes (X, Y and Z) controlled by the LDV software. The Y position corresponds to the elevation in the assembly along the bundle axis; X is the lateral position and Z the depth position. For each position, a mean velocity was calculated for an acquisition of 1,024 points and/or 20 seconds maximum. The depth measurement step (Z) was 0.5 mm in air.

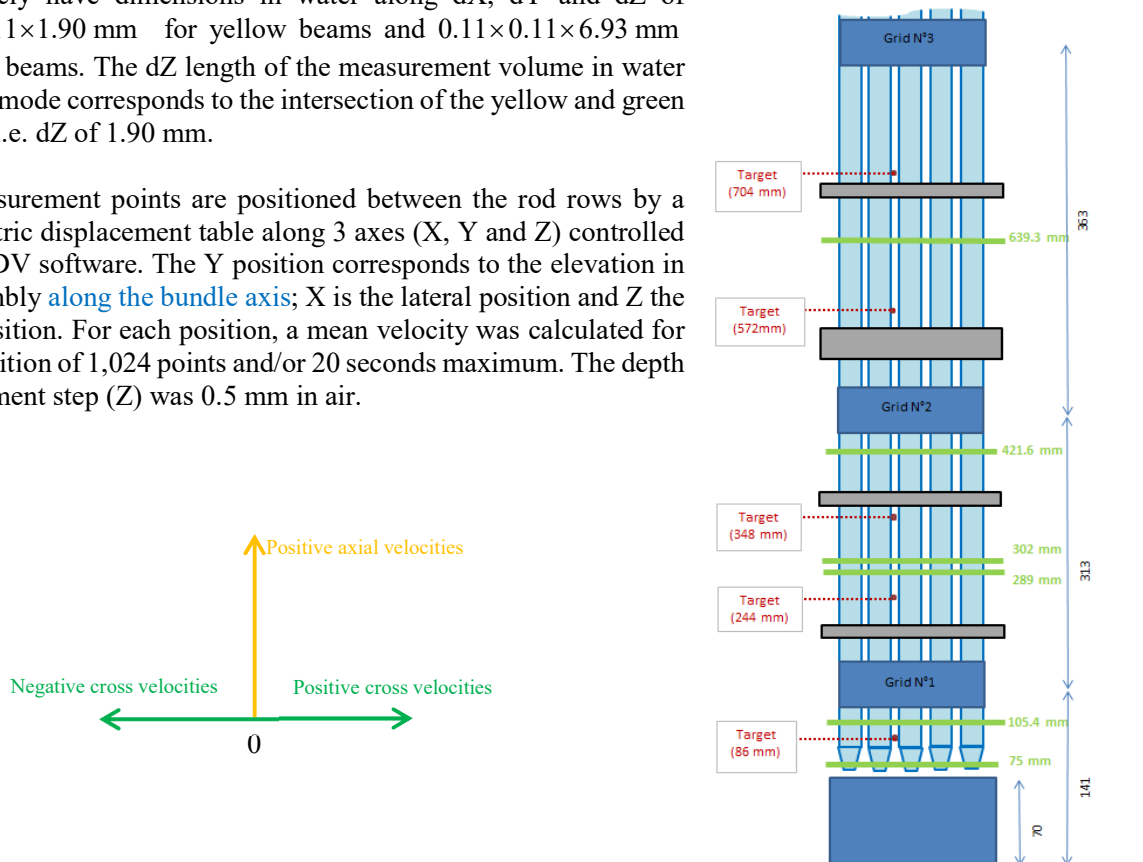
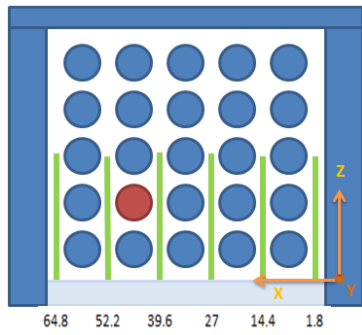


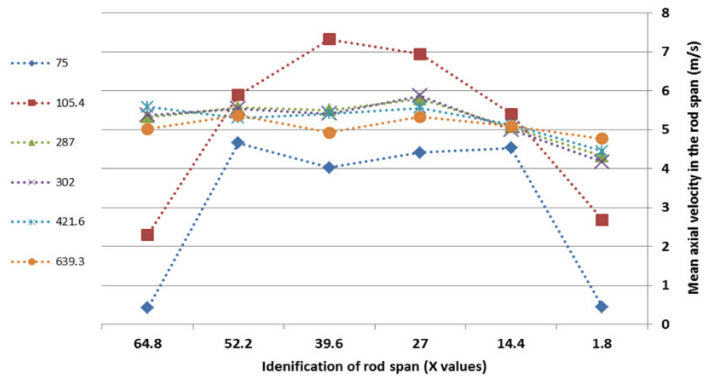
Figure 2. Velocity measurement orientations (left) and locations (right).

**Velocity measurements**

The flow rate entering the test section is adjusted to obtain a mean flow velocity of 5 m/s inside the rod bundles. Figure 3 provides velocity measures for several elevations, for one of the bundles, in terms of mean velocity for each inter-rod gap (along X) and for a half the bundle depth along Z. Velocity profiles below the first grid are heterogeneous, the spans close to the boundary of the bundles (X=1.8 and X=64.8) being significantly *under-supplied* compared to the others spans.



(a) Location of the mean velocity measurements (in red, the rod of interest for vibratory measures)



(b) Mean axial velocity in the rod span, for each elevation (along Y)

Figure 3. Axial velocity measurements.

Figure 4 presents the velocities in the vicinity of the rod of interest for vibrometry (see Figure 3), which show variations along the depth of the bundle (Z axis) for the lowest elevations. The mean velocity at these elevations generally exceeds 6 m/s. The expected mean velocity of 5 m/s is stabilized for the corresponding spans only above the second grid (Y=639.9 mm). Concerning cross velocities, the maximum fluctuations occur again close to the bottom of the rod (Y=75 mm et Y=105.4 mm).

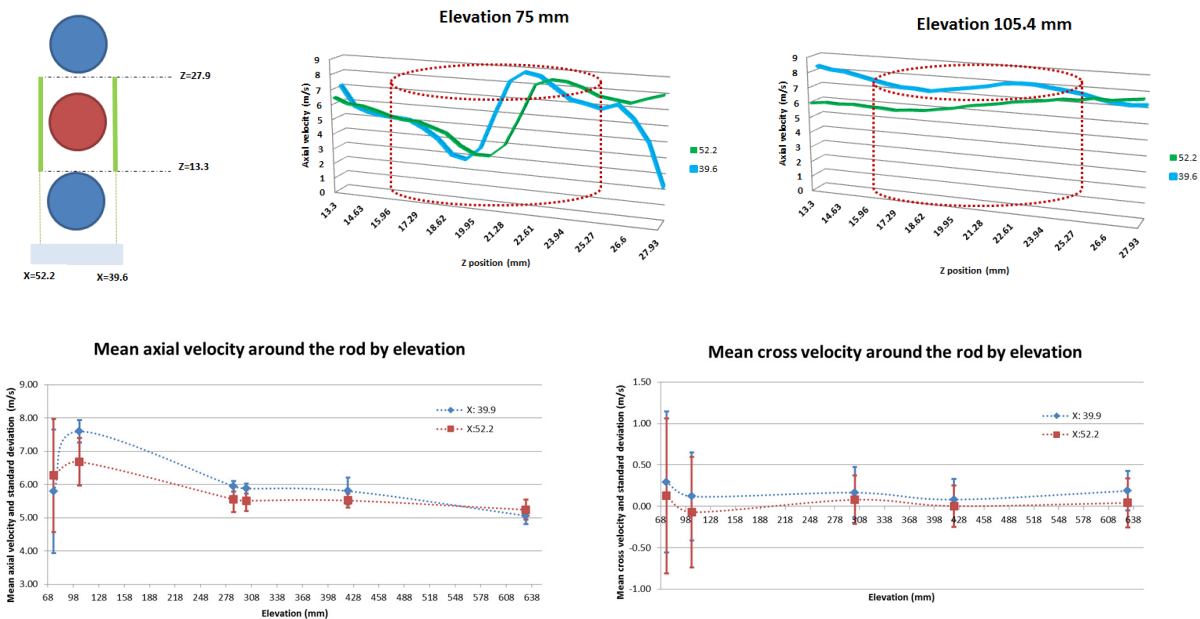


Figure 4. Velocity measures along the rod of interest for the vibrometry.

The measured axial velocity profile is in rather good accordance with the effective velocity profile identified from vibratory experiments (Part 1 - Antunes et al., 2017) and recalled for convenience in Figure 5. We recall that this effective velocity profile accounts for the total flow velocity, both axial and transverse, however the cross velocity proves to remains small in the measures.

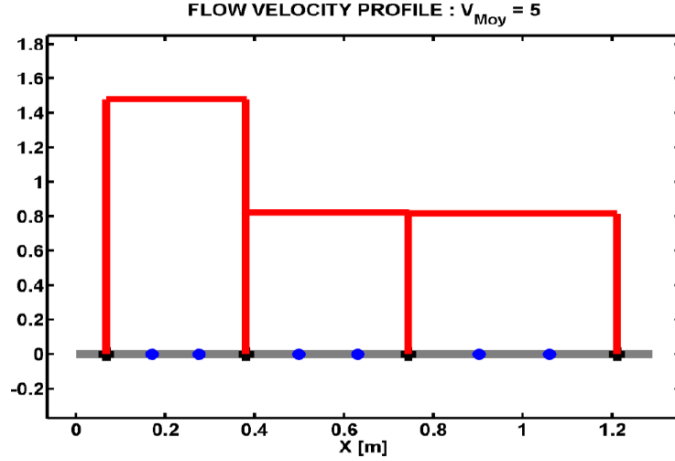


Figure 5. Velocity profile along the instrumented rod identified from vibratory experiments (Part 1 - Antunes et al., 2017).

## VIBRATION COMPUTATIONS

### Computational procedures

Techniques for time-domain dynamical simulation of flow-excited tubular bundles have been developed by the authors and others for more than three decades. Here we briefly recall the essential features of the computational procedures used here for predicting the vibratory response of the fuel rod, see by Axisa et al. (1988), Antunes et al. (2011 and 2012) and Piteau et al. (2012) for further details. A classic modal discretization approach is adopted for modelling the rod motions along the two orthogonal transverse directions  $X$  and  $Z$  (see Figure 3):

$$\begin{cases} m_n^X \ddot{q}_n^X(t) + c_n^X \dot{q}_n^X(t) + k_n^X q_n^X(t) = F_n^X(t) \\ m_n^Z \ddot{q}_n^Z(t) + c_n^Z \dot{q}_n^Z(t) + k_n^Z q_n^Z(t) = F_n^Z(t) \end{cases}, \quad n = 1, 2, \dots, N \quad (1)$$

with the modal parameters  $c_n^{X,Z} = 2m_n^{X,Z} \omega_n^{X,Z} \zeta_n^{X,Z}$  and  $k_n^{X,Z} = m_n^{X,Z} (\omega_n^{X,Z})^2$ , where the modal masses  $m_n^{X,Z}$  and modal frequencies  $\omega_n^{X,Z}$  incorporate the added inertia effect from the fluid, while the modal damping coefficients  $\zeta_n^{X,Z}$  incorporate dissipation due to the fluid viscosity. The physical responses are recovered from the computed modal responses through modal summation:

$$X(x,t) = \sum_{n=1}^N \phi_n^X(x) q_n^X(t) \quad ; \quad Z(x,t) = \sum_{n=1}^N \phi_n^Z(x) q_n^Z(t) \quad (2)$$

where  $\phi_n^{X,Z}(x)$  are the modeshapes of the rod (unconstrained at the nonlinear supports). On the other hand, the modal forces  $F_n^{X,Z}(t)$  include the modal projection of the distributed flow forces  $F_n^{f_{X,Z}}(t)$ , and of the localized contact forces at the nonlinear supports  $F_n^{s_{X,Z}}(t)$ :

$$F_n^{X,Z}(t) = F_n^{f_{x,z}}(t) + F_n^{s_{x,z}}(t) = \int_0^L F_f^{X,Z}(x,t) \phi_n^{X,Z}(x) dx + \sum_{s=1}^S \int_0^L F_s^{X,Z}(t) \delta(x-x_s) \phi_n^{X,Z}(x) dx$$

$$\approx \int_0^L F_{tur}^{X,Z}(x,t) \phi_n^{X,Z}(x) dx + \sum_{s=1}^S F_s^{X,Z}(t) \phi_n^{X,Z}(x_s) \quad , \quad n = 1, 2, \dots, N$$
(3)

The flow force field encapsulates both the fluidelastic coupling and turbulence effects,  $F_f^{X,Z}(x,t) = F_{fe}^{X,Z}(x,t) + F_{tur}^{X,Z}(x,t)$ . However, the fluidelastic effects connected with the axial flow can be safely postulated as negligible, so that only the random turbulence excitation  $F_{tur}^{X,Z}(x,t)$  is addressed.

Time-domain realizations of the modal forces  $F_n^{f_{x,z}}(t)$  were directly generated from the space-frequency turbulence model discussed in Part 1, using the effective technique developed by Antunes et al. (2016), which preserves both the frequency content and the space correlation of the distributed turbulence excitation. In the simplified theoretical framework developed in Part 1, for an axial, or transverse or mixed flow, given a reference flow velocity  $\bar{V}$  and a dimensionless equivalent reference excitation spectrum  $\hat{\Phi}_{EQR}(\bar{f}_R)$ , the cross-spectra between any two modal excitations are given as:

$$S_{F_n F_m}(f) = \left( \frac{1}{2} \rho \bar{V}^2 D \right)^2 \frac{D}{\bar{V}} \hat{\Phi}_{EQR} \left( \frac{fD}{\bar{V}} \right) C_{nm}^2 = \Phi_{FF}(f) C_{nm}^2 \quad , \quad m, n = 1, 2, \dots, N \quad ; \quad \bar{f}_R = \frac{fD}{\bar{V}} \quad (4)$$

with the simplified cross-correlation integrals:

$$C_{nm}^2 = 2 \int_0^L \phi_n(x) \phi_m(x) [u(x)]^4 dx \quad , \quad m, n = 1, 2, \dots, N \quad (5)$$

where  $u(x)$  is the flow velocity profile. Then, the following matrix of modal cross-spectra may be built:

$$[\mathbf{S}_{FF}(f)] = \begin{bmatrix} S_{F_1 F_1}(f) & S_{F_1 F_2}(f) & \dots & S_{F_1 F_N}(f) \\ S_{F_2 F_1}(f) & S_{F_2 F_2}(f) & \dots & S_{F_2 F_N}(f) \\ \vdots & \vdots & \ddots & \vdots \\ S_{F_N F_1}(f) & S_{F_N F_2}(f) & \dots & S_{F_N F_N}(f) \end{bmatrix} = \Phi_{FF}(f) \begin{bmatrix} C_{11}^2 & C_{12}^2 & \dots & C_{1N}^2 \\ C_{21}^2 & C_{22}^2 & \dots & C_{2N}^2 \\ \vdots & \vdots & \ddots & \vdots \\ C_{N1}^2 & C_{N2}^2 & \dots & C_{NN}^2 \end{bmatrix} = \Phi_{FF}(f) [\mathbf{C}^2] \quad (6)$$

and, as shown by Antunes et al. (2016), suitable modal excitation time-histories can be computed as:

$$F_n(t) = \alpha \sum_{l=1}^N \{ \Psi^l \} FFT^{-1} \left( \sqrt{\Phi_{FF}(f) \lambda_l} \exp(-i\varphi_l(f)) \right) \quad (7)$$

where constant  $\alpha = N_T \sqrt{\Delta f / 2}$  is related to the signals discretization (frequency resolution  $\Delta f$  and  $N_T$  time samples),  $\varphi_l(f)$  are random phases uniformly distributed in the range  $[0, 2\pi]$ , while the columns  $\{ \Psi^l \}$  of  $[\Psi]$  and the diagonal terms  $\lambda_l$  of  $[\Lambda]$  are obtained from the eigen-decomposition of  $[\mathbf{C}^2]$ :

$$[\mathbf{C}^2][\Psi] = [\Psi][\Lambda] \quad (8)$$

### Computational results

Following the previously described computational model, dynamical time-domain simulations were performed for the reference velocity  $\bar{V} = 5$  m/s, using the identified velocity profile  $u(x)$  shown in Figure 5 and the identified dimensionless equivalent reference excitation spectrum  $\hat{\Phi}_{EQR}(\bar{f}_R)$  of Figure 6. Computations were performed based on the rod unconstrained modes at the supports, using the parameters shown in Figure 7, where P is the inter-rods gap, D the rod diameter, L the total length, E the Young's

modulus,  $m_0$  the mass per unit length (including fluid inertia),  $F_{axi}$  the axial preloading force and  $\zeta_n$  the modal damping (assumed identical for all modes). As shown in Figure 7, the four supporting grids at nominal axial locations  $Y_g$  are composed of two orthogonal sets, each one composed by a preloading spring ( $S$ ) and two dimples ( $P$ ) at distance  $L_x = L_z$ . The stiffness constants  $K_r$ ,  $K_t$  and  $K_a$  of the springs and dimples, along the radial, tangential and axial directions, were obtained from a detailed local FEM analysis. In particular, preloading of the springs resulted in the estimated preloads  $F_x = F_z$ . Under such conditions, for the vibration amplitudes of the present tests, it was found that any friction coefficient higher than would 0.1 prevent significant sliding. Therefore, the friction coefficients used for our computations are not critical and we believe they lead to representative results.

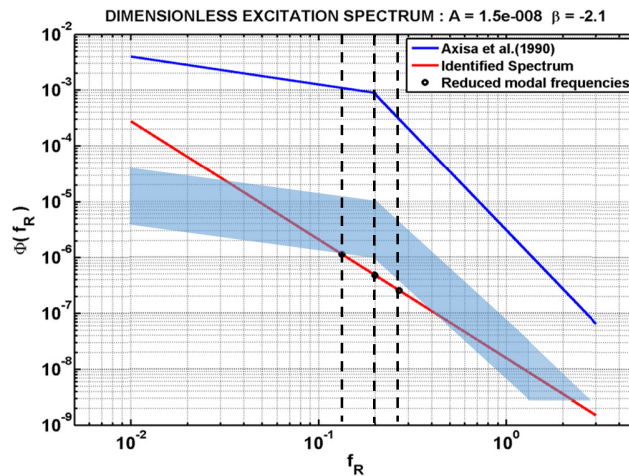


Figure 6. Identified dimensionless equivalent reference excitation spectrum (Part 1 - Antunes et al., 2017).

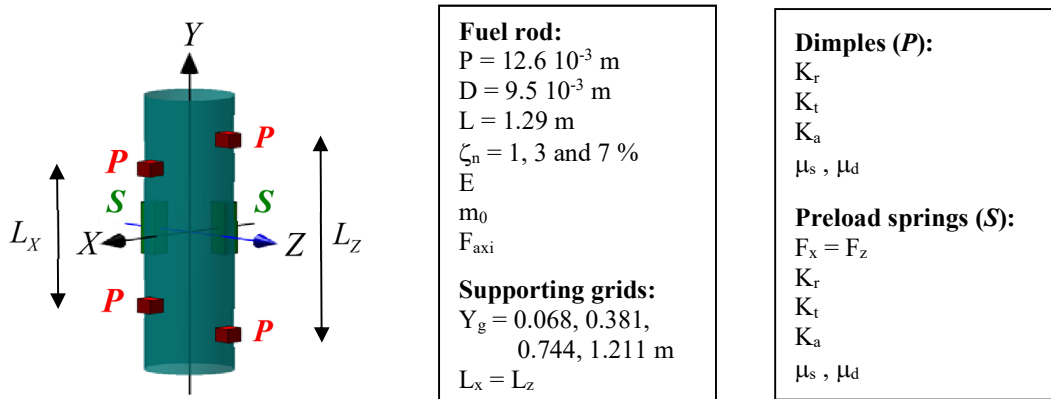


Figure 7. Modelling of the rod supports.

From this computational data, Figure 8 displays the computational flow velocity profile and compares the measured and computed results, concerning the RMS response amplitude along the rod, the modal response frequencies and modal damping coefficients of the support-constrained modes. The various results pertain to the SOBI-identified measurements, as well as computations performed assuming modal damping values of  $\zeta_n = 1, 3$  and  $7 \%$ , for all the unconstrained modes of the computational basis. The resulting modal frequencies of the support-constrained modes are essentially insensitive to the any changes in the computational parameters, however such is not the case for the response amplitude and modal damping of the support-constrained system. These results highlight that, in order to obtain similar experimental and

computed results, a somewhat large value must be assumed for the rod modal damping (7 %), which is however entirely compatible with the experimentally identified damping of the test rod.

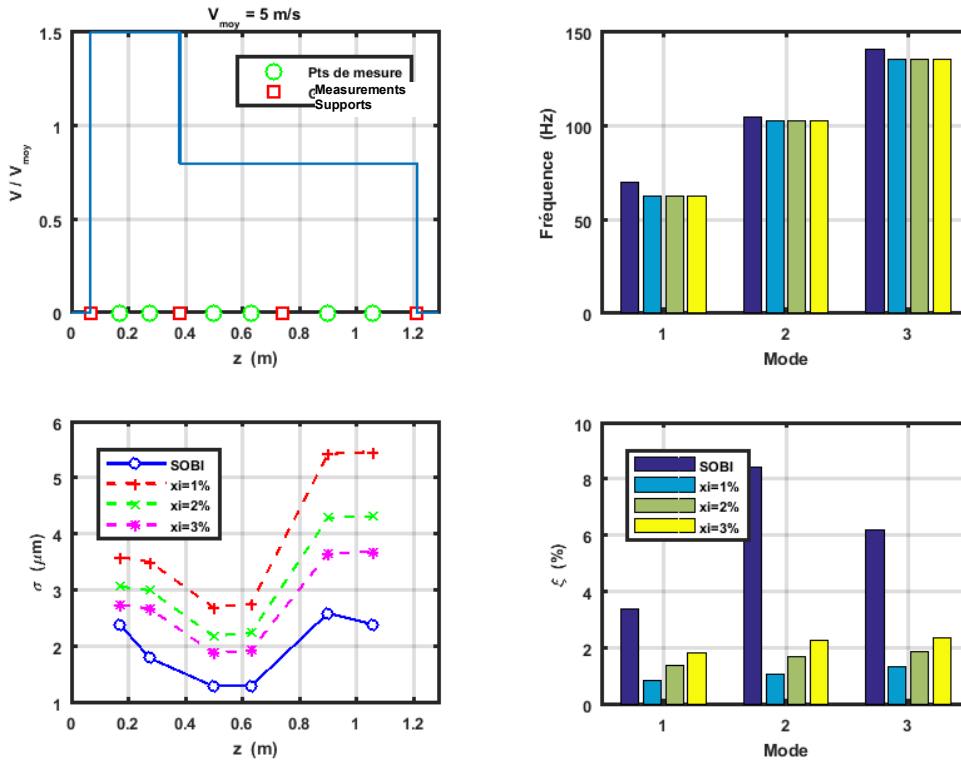


Figure 8. Experimental and computed results as a function of the assumed computational modal damping values: Flow velocity profile (*upper-left plot*); RMS response amplitude along the rod (*lower-left plot*); Modal frequencies of the support-constrained modes (*upper-right plot*); Modal damping coefficients of the support-constrained modes (*lower-right plots*).

The plots in Figure 9 demonstrate that, as mentioned earlier, for the low vibratory level of the present experiments, results are also nearly insensitive to the friction coefficient at the supporting fixtures. Here the computational levels are higher than in the experiments, as the computations were performed with modal damping values of 1 %, much lower than the experimental damping. In conclusion, the present results indicate that the most sensitive modelling parameter is modal damping. Moreover, the experimental results are satisfactory reproduced if a suitable value of  $\zeta_n$  is used, which is compatible with the experimentally identified damping.

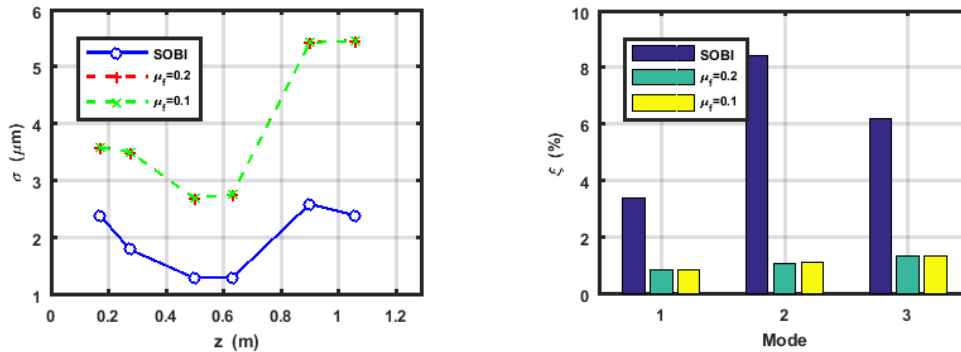


Figure 9. Experimental and computed results as a function of the assumed friction coefficients: Flow velocity profile (*left plot*); modes (*right plot*).

## CONCLUSION

With respect to the test rig studied in Part 1 - Antunes et al. (2017), we present in this paper Laser Doppler Velocimetry measurements of the flow as well as dynamical computations of the turbulence-excited vibrating rod. The supplementary results thus obtained validate the identified flow velocity profile and turbulence excitation spectrum, which constitute the main flow features obtained in Part 1. As pointed, the present investigation concerned a particularly problematic flow-excited system, due to the noisy data. Nevertheless, a severely constrained source identification strategy achieved seemingly credible results, which have been further solidified through the analysis presented in Part 2.

## ACKNOWLEDGEMENTS

The authors wish to thank AREVA and Electricité de France (EDF) for their support and contribution.

## REFERENCES

- Antunes, J., Delaune, X. and Piteau, P. (2011). "Time-Domain Modeling of the Random Vibrations of Tubes Subjected to Turbulence-Conveying Flows", *ASME Pressure Vessel and Piping Conference (PVP-2011)*, Baltimore, USA.
- Antunes, J., Borsoi, L., Piteau, P. and Delaune, X. (2012). "The Equivalent Spectrum Concept for Turbulence Conveying Excitations", *10th International Conference on Flow-Induced Vibration & Flow-Induced Noise (FIV-2012)*, Dublin, Ireland.
- Antunes, J., Piteau, P., Delaune, X. and Borsoi, L. (2016). "A New Method for the Generation of Representative Time-Domain Turbulence Excitations", *Journal of Fluids and Structures*, Vol. 58, pp. 1-19.
- Antunes, J., Biscay, V., Piteau, P., Delaune, X., Vivet, A., and Faucher, V. (2017). "Experimental Identification of Flow Turbulence Excitations in a Fuel Bundle Test Rig: Part 1 - Experiments and Source Identification from Low Amplitude Rod Vibrations", *24th International Conference on Structural Mechanics in Reactor Technology (SMiRT-24)*, Busan, South Korea.
- Axisa, F., Antunes, J. and Villard, B. (1988). "Overview of Numerical Methods for Predicting Flow-Induced Vibration of Heat Exchanger Tube Bundles", *ASME Journal of Pressure Vessel Technology*, Vol. 110, pp. 6-14.
- Eder, A., Durst, B. and Jordan, M. (2001). "Laser-Doppler Velocimetry - Principle and Application to Turbulence Measurements", in *Optical Measurements: Techniques and Applications* (F. Mayinger, O. Feldmann, Eds.), Springer-Verlag, Berlin, Germany.
- Piteau, P., Delaune, X., Antunes, J. and Borsoi, L. (2012). "Experiments and Computations of a Loosely Supported Tube in a Rigid Bundle Subjected to Single-Phase Flow", *Journal of Fluids and Structures*, Vol. 28, pp. 56-71.